Dynamic modeling and control of a novel *XY* positioning stage for semiconductor packaging

Wang Fujun[1, 2], Ma Zhipeng[1], Gao Weiguo[1*], Zhao Xingyu[1], Tian Yanling[1], Zhang Dawei[1], and Liang Cunman[1]

1 Tianjin Key Laboratory of Equipment Design and Manufacturing Technology, School of Mechanical Engineering, Tianjin University, Tianjin 300072, China

2 Department of Mechanical Science and Engineering, University of Illinois at Urbana-Champaign, Urbana, IL 61801, USA

Abstract: This paper presents the dynamic modeling and controller design of an *XY* positioning stage for semiconductor packaging. The *XY* stage is directly driven by two linear voice coil motors (LVCMs), and motion decoupling between the *X*- and *Y*- axes is realized through a novel flexible decoupling mechanism based on flexure hinges and preloaded spring. Through bond graph method, the dynamic models of *X*- and *Y*-axes servomechanisms are established, respectively and the state space equations are derived. A control methodology is proposed based on force compensations and the performance of the *XY* stage is investigated by simulations and experimental tests. The results show that the *XY* stage has good performance. When the reference displacements are defined as 2 mm, the settling time of the *X*-axis movement is 64 ms, and the overshoot is 0.7%. *Y*-axis settling time is 62 ms, and the overshoot is 0.8%. *X*-axis positioning accuracy is 1.85 μm and the repeatability is 0.95 μm. *Y*-axis positioning accuracy and repeatability are 1.75 μm and 0.9 μm, respectively. In addition, the stage can track linear, circular and complex trajectories very well.

Keywords: *XY* positioning stage, Dynamic modeling, Control

*Corresponding author: Tianjin Key Laboratory of Equipment Design and Manufacturing Technology,

School of Mechanical Engineering, Tianjin University, 92 Weijin Road, Nankai District, Tianjin 300072, China. Email: gaowg@tju.edu.cn, Tel./fax: +86 022 87401950

1 Introduction

Recently the trend towards miniaturizing semiconductor products such as integrated chips and MEMS has stimulated extensive research on semiconductor packaging (Li and Xu, 2011; Aized and Shirinzadeh, 2011; Liaw and Shirinzadeh, 2008; Fatikow et al., 2008; Zhang et al., 2013; Wang et al., 2009). As one of the essential components of semiconductor packaging machines, high speed *XY* positioning stage with a micro scale resolution and motion stroke of over several millimeters plays an important role in the packaging process (Wang et al., 2011; Hwang et al., 2010; Liang et al., 2010; Wang et al., 2014).

Numerous new drive technologies (e.g., piezoelectric, electrostatic, etc.) have been utilized in the *XY* positioning stages (Tian et al., 2009; Li and Xu, 2011). However, electromagnetic actuation is still considered to be the best choice for the motion with a long stroke of more than several millimeters (Khan et al., 2011). Most traditional *XY* stages equipped with rotational motors and ball screws have disadvantages of reduced accuracy, complex mechanical structure and low reliability, and it can not meet the stringent requirements of precision manufacturing and assembly industry (Hace et al., 2011; Liu et al., 2003). Direct-drive motors have the advantages of low friction and high mechanical stiffness, and thus they have been increasingly used in the high speed precision positioning *XY* stage (Dejima et al., 2005; Sanchez and Ricolfe, 2012). Consequently, it is very essential to study on the dynamic modeling and controller

design of the direct-drive stage to cope with the increasingly demanding requirements.

Dynamic model is the basic of dynamic analysis and controller design, so many researchers have been working on the dynamic modeling and analysis of *XY* stages. Teo et al. (2007) and Zhao et al. (2010) established the dynamic models of the mechanical system of an H-type gantry direct-drive stages using Lagrangian equation. Cai et al. (2011) carried out the dynamic modeling of a 3-DOF ultra-precision positioning stage with air bearing through rigid body finite rotation Jourdain Principle and the vibration frequency and mode were analyzed and discussed. A numerical method based on mechanical energy conservation was adopted to calculate the undamped natural frequency of a parallel-kinematic positioning *XY* stage (Ferreira et al., 2007). Fung et al. (2009) achieved the dynamic model of a dual-stage *XY* precision positioning table with the aid of analytical method and experimental identification approach. The high speed precision positioning *XY* stage is a complex system which integrates mechanical, electrical and other physical processes. During the high speed motion with short strokes, *XY* stage usually shows the characteristics of high order, multi variables and time-varying, so the dynamic behavior of the *XY* stage becomes extremely complex. The dynamic model obtained through the above traditional theoretical modeling methods can not accurately demonstrate the actual dynamic behavior of such complex systems. As a global dynamic modeling method, bond graph represents the system in terms of energy and information flow, and the advantage of this method is that the dynamic model in multi-energy domains can be constructed in a rather small set of ideal elements (Wang et al., 2009; Sun et al., 2011). As a result, it is very suitable for the

dynamic modeling and characteristic analysis of high-speed and high-accuracy positioning *XY* stage.

The controller is one of the important elements of an *XY* positioning stage, because of its ability to eliminate positioning errors. In the literature, proportion-integration-differentiation (PID) compensator is by far the most widely used form of feedback controller (Ang et al., 2005). However, it can not meet the increasingly stringent performance requirements of the high speed *XY* positioning stage (Liu, et al. 2005). Ding et al. (2006) presented a combination of friction compensator and disturbance observer (DOB) to eliminate the uncompensated friction and other external disturbances for a direct-drive stage. Tomizuka (1987) proposed a zero phase error tracking controller (ZPETC) based on approximate inversion of the closed-loop system to eliminate time delay disturbance and improve tracking performance of an *XY* stage. Several advanced control theories including the adaptive robust control (ARC) (Xu and Yao, 2000), variable-structure control (VSC) (Adamy and Flemming, 2004), iterative learning control (Wu and Ding, 2007), fuzzy control (Mou and Sung, 2012) and neural networks control (Xu and Li, 2012), were proposed to control direct-drive positioning stages, and they can provide appropriate level of performance. However, their applications are limited in industry applications by the expensive algorithms and calculations. In addition, these studies mostly focused on linear motor direct-drive *XY* stages.

In this paper, the dynamic modeling and controller design of a precision positioning *XY* stage for semiconductor packaging are presented. Firstly we describe the

configuration of the *XY* stage with a novel decoupling mechanism. Then considering the characteristics of the servomechanism, the dynamic model is established using bond graph method. On the basis of force compensation principle, the controller is designed. Finally the performance of the *XY* stage is evaluated by simulations and experimental tests.

2 Dynamic modeling of the *XY* stage

Prior to the modeling of the *XY* positioning stage, a brief description of the mechanism of the *XY* stage will provide a good basis for the subsequent discussion.

2.1 Mechanical structure

The mechanism of the LVCMs direct-drive *XY* stage is shown in Fig.1. The stage is mainly composed of *X*- and *Y*-axes LVCMs, *X*- and *Y*-axes tables, the motion decoupling mechanism and the base. Linear grating encoders are used as the feedback sensors for *X*- and *Y*-axes tables. The *X*- and *Y*-axes motors are both fixed on the base. *X*-axis table is connected with *X*-axis LVCM by the pushing plate. *Y*-axis table is located above *X*-axis table, and it is also connected to the *Y*-axis LVCM by the motion decoupling mechanism. The *Y*-axis motor is connected to the guiding fin which can move in *Y* axis on the sliding guides. One end of the preloaded connecting rod is mounted on the guiding fin and the other end is connected to the preload spring. The preload spring is also mounted on the guiding fin. The front and back roller bearings are mounted on the guiding fin and roll contact the front and back lapping plates, respectively.

The decoupling mechanism is composed of the guiding fin, preloaded connecting

rod, back roller bearing, front roller bearing, back lapping plate, front lapping plate, flexure hinges and the preloaded spring. The Y-axis LVCM is connected to the guiding fin which can move in *Y* axis on the sliding guides. One end of the preloaded connecting rod is mounted on the guiding fin and the other end is connected to the preload spring. The preload spring is also mounted on the guiding fin. The front and back roller bearings are mounted on the guiding fin and roll contact with the front and back lapping plates, respectively.

The *Y*-axis motor generates a force, which will drive the *Y*-axis table by the flexible decoupling mechanism. When *X*-axis motor generates a force, the Y-axis table will move with *X*-axis table in *X* direction, the front and back roller bearings roll along the front and back lapping plate separately, and thus the motion decoupling of *X*- and *Y*-axes is realized. Thus the motion mass can be greatly reduced. Moreover, the dynamic load and the residual vibrations during high speed motion and the instant interference generated when *X*- and *Y*-axes motion at the same time can be suppressed by the slight deformation of flexure hinges.

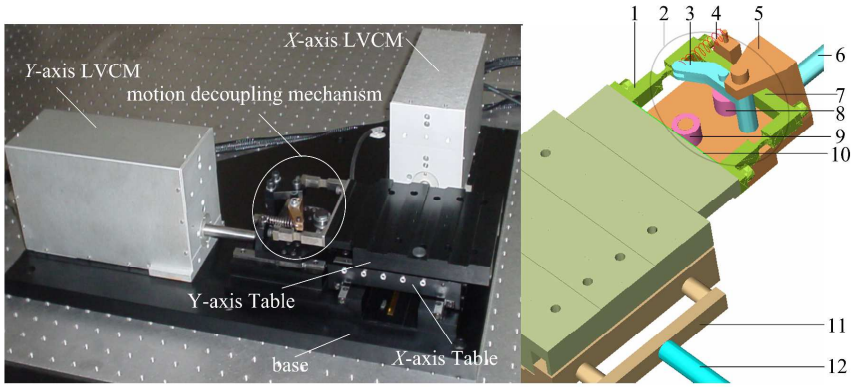

1-flexure hinges, 2-decoupling mechanism, 3-preloaded connecting rod, 4-preloaded spring, 5-guiding fin, 6-*Y*-axis VCM shaft, 7-front lapping plate, 8-front needle roller, 9-back needle roller, 10-back lapping plate, 11-pushing plate, 12-*X*-axis VCM shaft.

Fig.1 The configuration of the LVCMs direct-drive *XY* stage.

2.2 Dynamic modeling using bond graph method

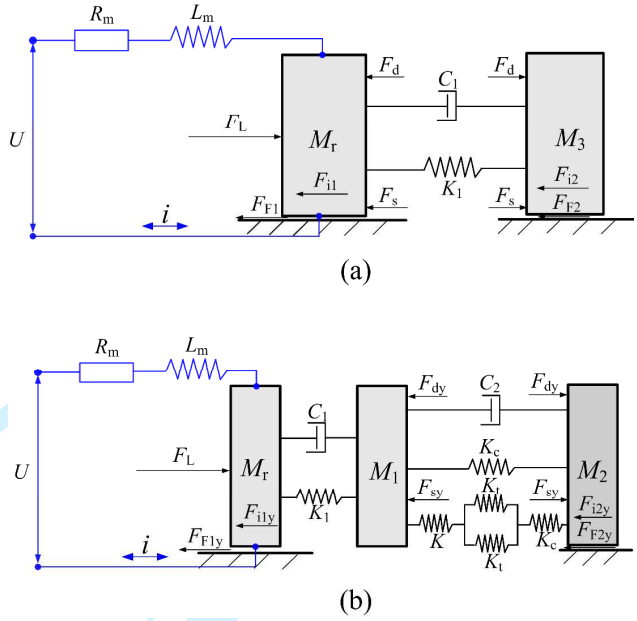

Fig.2 The dynamic model of the LVCMs direct-drive *XY* stage: (a) for *X*-axis, and (b) for *Y*-axis.

The dynamic model of the VCMs direct-drive *XY* stage is shown in Fig.2, where U is the voltage applied to the VCM, R_m is the resistance of the VCM coil, i is the current intensity through the coil, L_m is the inductance of the VCM coil, M_r is the mass of the coil, M_1 and M_2 are the equivalent mass of the *Y*-axis guiding fin and table, respectively, M_3 is the mass of the *X*-axis table, K_1 and C_1 are the connecting stiffness and damping between coil and the guiding fin, respectively, K is the stiffness of the preload spring, K_t is the stiffness of the flexure hinge, K_c is the contact stiffness between the bearing and the lapping plate, C_2 is the equivalent damping between the *Y*-axis guiding fin and table, F_L is the output force of the coil, F_d is the *X*-axis damping force, F_s is the *X*-axis equivalent spring force, F_{dy} is the *Y*-axis damping force, F_{sy} is the *Y*-axis equivalent spring force, F_{F1} is the friction of the *X*-axis coil, F_{F2} is the friction of the *X*-axis table, F_{F1y} is the friction of the *Y*-axis coil, F_{F2y} is the friction of the *Y*-axis table, F_{i1} is the

inertia force of the *X*-axis coil, F_{i2} is the inertia force of the *X*-axis table, F_{i1y} is the inertia force of the *Y*-axis coil, and F_{i2y} is the inertia force of the *Y*-axis table.

A VCM is basically an electromagnetic transducer in which a coil is placed in a magnetic pole gap experiences a force proportional to the current passing through the coil. Assuming that the force generated by the VCM is independent of the position, the governing equations can be written as equations (1) and (2)

$$U = R_m i + L_m \frac{di}{dt} + K_B v \qquad (1)$$

$$F = K_F i = M_r \frac{dv}{dt} + F_L \qquad (2)$$

where v is the motion velocity of the VCM coil, F is the force generated by the VCM, K_B is the coefficient of inducted electromotive force, and K_F is the force coefficient.

The dynamics of the *X*- and *Y*- axes servomechanism is represented by the following second-order linear differential equations.

$$M_3 \frac{d^2x}{dt^2} + C_1 \frac{dx}{dt} + K_1 x = F_L - F_{F2} \qquad (3)$$

$$M_y \frac{d^2y}{dt^2} + C_y \frac{dy}{dt} + K_y y = F_y \qquad (4)$$

where x is the displacement of *X*-axis table, $M_y = \begin{bmatrix} M_1 & 0 \\ 0 & M_2 \end{bmatrix}$, $C_y = \begin{bmatrix} C_1 + C_2 & -C_2 \\ -C_2 & C_2 \end{bmatrix}$,

$K_y = \begin{bmatrix} K_1 + K_{y2} & -K_{y2} \\ -K_{y2} & K_{y2} \end{bmatrix}$, $y = \begin{bmatrix} y_1 \\ y_2 \end{bmatrix}$, $F_y = \begin{bmatrix} F_L \\ -F_{F2} \end{bmatrix}$, $K_{y2} = \frac{2K_t K_r K_c}{2K_t K + 2K_t K_c + K K_c} + K_c$,

y_1 and y_2 are the displacements of *Y*-axis guiding fin and table, respectively.

Exponential friction model is adopted, and it can be expressed as

$$F_F(v_f) = signum(v_f) \cdot (F_c + (F_{st} - F_c) \cdot e^{-\left|\frac{v_f}{v_s}\right|^2}) + \mu v_f \qquad (5)$$

where v_f is velocity, F_c is coulomb friction, F_{st} is static friction, v_s is Stribeck velocity,

and μ is viscous friction coefficient.

Bond graph is an explicit graphical tool for capturing the common energy structure of systems, and by this approach, a physical system can be represented by symbols and lines, identifying the power flow paths. The basic variables in bond graph are effort (*e*), flow (*f*), time integral of effort (*p(t)*) and the time integral of flow (*q*(*t*)). Based on the principle of bond graph method, the output force of VCM is defined as the effort source ($\boldsymbol{S}_e$), the connecting damping and friction are defined as resistor elements (***R***), and the connecting stiffness is defined as capacitor element (***C***). Thus the bond graph for *X*- and *Y*- axes servomechanism can be obtained, and they are described in Fig.3(a) and Fig.3(b), respectively.

In *Y*-axis bond graph, according to the 1-junction that connects the bonds of 8, 9 and 10, the following equation can be gotten.

$$F_L = K_1 q_9 + \mathrm{C}_1 v_{10} \qquad (6)$$

Considering the 0-junction that connects the bonds of 7, 8 and 11, the following equation can be obtained.

$$v_{10} = v_r - v_1 = v_r - \frac{dy_1}{dt} \qquad (7)$$

Considering the 0-junction that connects the bonds of 13, 14 and 17, the following equation can be gotten.

$$v_{16} = v_1 - v_2 = \frac{dy_1}{dt} - \frac{dy_2}{dt} \qquad (8)$$

Considering the 1-junction that connects the bonds of 11, 12 and 13 and the 1-junction that connects the bonds of 17, 18 and 19, the following equation can be

achieved.

$$F_L = M_1 a_{12} + M_2 a_{18} + f(v_{19}) + \mu v_{19} \qquad (9)$$

And

$$f(v_{19}) = signum(v_{19})(F_c + (F_{st} - F_c)e^{-\left|\frac{v_{19}}{v_s}\right|^2}) \qquad (10)$$

According to the 1-junction that connects the bonds of 14, 15 and 16, the following equation can be gotten.

$$F_L - M_1 a_{12} = K_{eq} q_{15} + C_2 v_{16} \qquad (11)$$

where $K_{eq} = K_c + \dfrac{2K_t K K_c}{2K_t + K + K_c}$

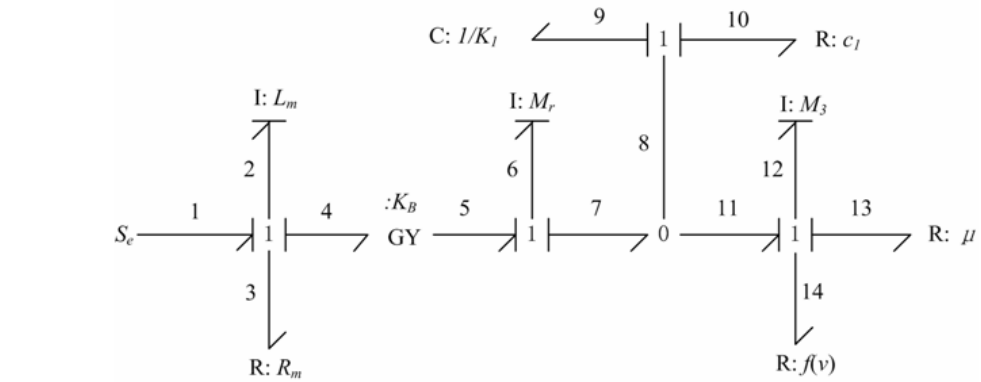

(a)

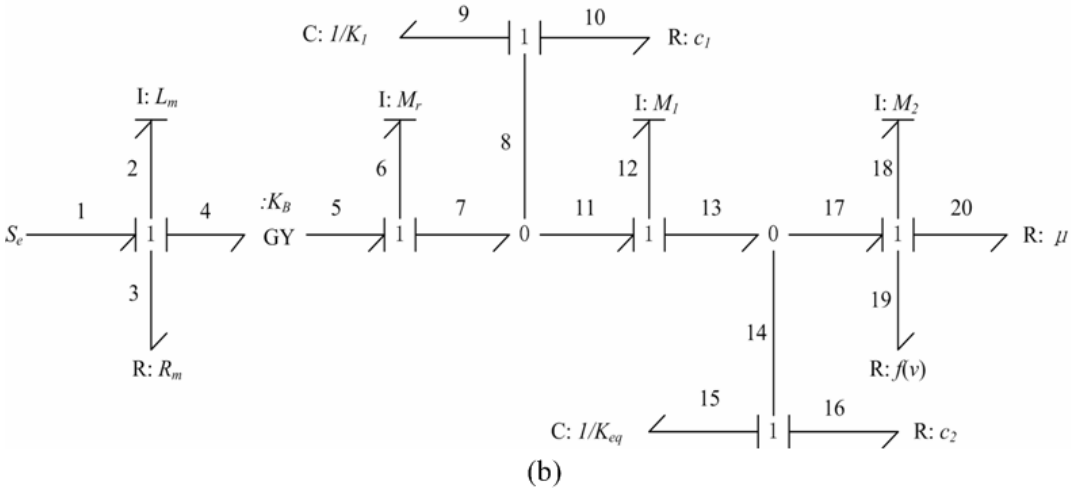

(b)

Fig.3 The bond graph of the LVCMs direct-drive *XY* stage: (a) for *X*-axis, and (b) for *Y*-axis.

Considering the inertia and capacitance effects have great significances to the dynamic performance of the system, the generalized momentum $p(t)$ of inertia element and generalized displacement $q(t)$ are selected as the state variables of the *XY* stage.

X-axis state variables can be expressed as

$$\boldsymbol{x}_x = \begin{bmatrix} p_2 & p_6 & q_9 & p_{12} \end{bmatrix}^T = \begin{bmatrix} f_2 L_m & f_6 M_r & \dfrac{e_9}{K_1} & f_{12} M_3 \end{bmatrix}^T \tag{12}$$

The input variable $\boldsymbol{u}_x = \begin{bmatrix} e_1 \end{bmatrix}$, and the output variable is $\boldsymbol{y}_x = \begin{bmatrix} f_{12} \end{bmatrix}$. According to the relation of the power flow and the definition of basic elements, the *X*-axis state space equation and output equation can be gotten, and they are written as

$$\dot{\boldsymbol{x}}_x = \boldsymbol{A}_x \boldsymbol{x}_x + \boldsymbol{B}_x \boldsymbol{u}_x \tag{13}$$

$$\boldsymbol{y}_x = \boldsymbol{C}_x \boldsymbol{x}_x + \boldsymbol{D}_x \boldsymbol{u}_x \tag{14}$$

where $\boldsymbol{A}_x = \begin{bmatrix} -\dfrac{R_m}{L_m} & -\dfrac{K_B}{M_r} & 0 & 0 \\ \dfrac{K_B}{L_m} & -\dfrac{C_1}{M_r} & -K_1 & 0 \\ 0 & \dfrac{1}{M_r} & 0 & -\dfrac{1}{M_3} \\ 0 & \dfrac{C_1}{M_r} & 0 & -\dfrac{C_1 + \mu}{M_3} \end{bmatrix}$, $\boldsymbol{B}_x = \begin{bmatrix} 1 \\ 0 \\ 0 \\ 0 \end{bmatrix}$,

$\boldsymbol{C}_x = \begin{bmatrix} 0 & 0 & 0 & 0 & 0 & \dfrac{1}{M_3} \end{bmatrix}$, and $\boldsymbol{D}_x = 0$.

Y-axis state variables can be expressed as

$$\boldsymbol{x}_y = \begin{bmatrix} p_2 & p_6 & q_9 & p_{12} & q_{15} & p_{18} \end{bmatrix}^T = \begin{bmatrix} f_2 L_m & f_6 M_r & \dfrac{e_9}{K_1} & f_{12} M_1 & \dfrac{e_{15}}{K_{eq}} & f_{18} M_2 \end{bmatrix}^T \tag{15}$$

The input variable $\boldsymbol{u}_y = \begin{bmatrix} e_1 \end{bmatrix}$, and the output variable is $\boldsymbol{y}_y = \begin{bmatrix} f_{12} \end{bmatrix}$. The relation between the effort and flow variables of resistor elements in the *Y*-axis bond graph can

be described by

$$\boldsymbol{e}=\begin{bmatrix} e_3 & e_{10} & e_{16} & e_{19} & e_{20}\end{bmatrix}^T=\begin{bmatrix} f_3R_m & f_{10}C_1 & f_{16}C_2 & f(f_{12}) & \mu f_{20}\end{bmatrix}^T \qquad (16)$$

Based on the integral causal relations of the basic elements in the *Y*-axis bond graph, the following equation can be obtained.

$$\dot{\boldsymbol{x}}_y=\begin{bmatrix}\dot{p}_2 & \dot{p}_6 & \dot{q}_9 & \dot{p}_{12} & \dot{q}_{15} & \dot{p}_{18}\end{bmatrix}^T=\begin{bmatrix} e_2 & e_6 & f_9 & e_{12} & f_{15} & e_{18}\end{bmatrix}^T \qquad (17)$$

According to the relation of the power flow and the definition of basic elements, the *Y*-axis state space equation and output equation can be achieved, and they are written as

$$\dot{\boldsymbol{x}}_y=\boldsymbol{A}_y\boldsymbol{x}_y+\boldsymbol{B}_y\boldsymbol{u}_y \qquad (18)$$

$$\boldsymbol{y}_y=\boldsymbol{C}_y\boldsymbol{x}_y+\boldsymbol{D}_y\boldsymbol{u}_y \qquad (19)$$

where $\boldsymbol{A}_y=\begin{bmatrix} -\frac{R_m}{L_m} & -\frac{K_B}{M_r} & 0 & 0 & 0 & 0\\ \frac{K_B}{L_m} & -\frac{C_1}{M_r} & -K_1 & \frac{C_1}{M_1} & 0 & 0\\ 0 & \frac{1}{M_r} & 0 & -\frac{1}{M_1} & 0 & 0\\ 0 & \frac{C_1}{M_r} & K_1 & -\frac{C_1+C_2}{M_1} & -K_{eq} & \frac{C_2}{M_2}\\ 0 & 0 & 0 & \frac{1}{M_1} & 0 & -\frac{1}{M_2}\\ 0 & 0 & 0 & \frac{C_2}{M_1} & K_{eq} & -\frac{C_2+\mu}{M_1}\end{bmatrix}$, $\boldsymbol{B}_y=\begin{bmatrix}1\\0\\0\\0\\0\\0\end{bmatrix}$,

$\boldsymbol{C}_y=\begin{bmatrix}0 & 0 & 0 & 0 & 0 & \frac{1}{M_2}\end{bmatrix}$, and $\boldsymbol{D}_y=0$.

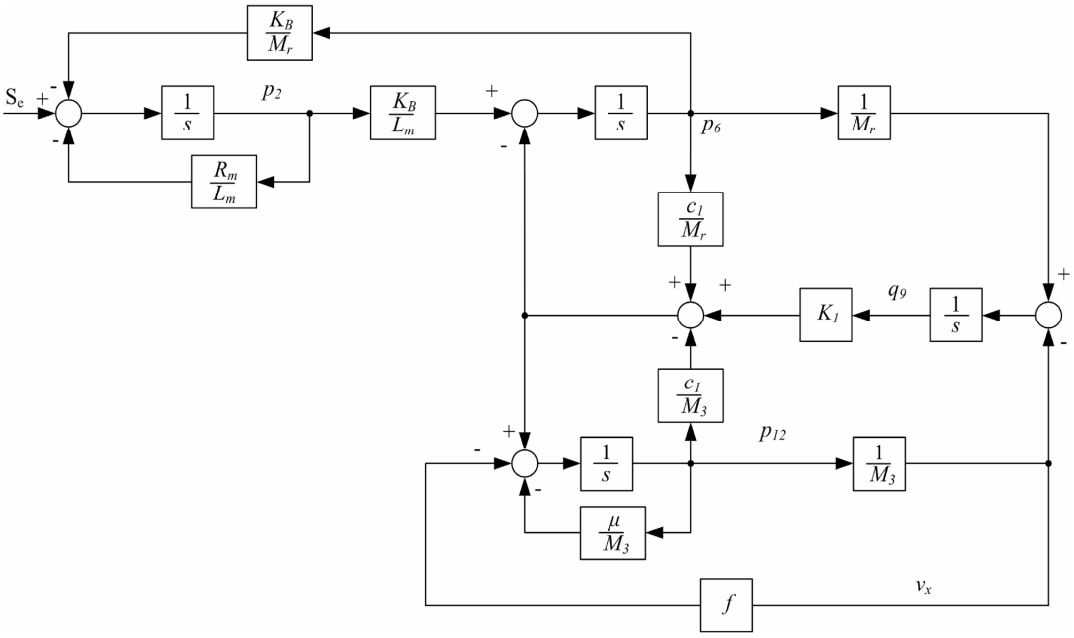

Fig.4 The global system control diagram for *X*-axis servomechanism.

Thus the global system control diagrams for *X*- and *Y*-axes servomechanisms can be established, and they are depicted in Fig.4 and Fig.5, respectively. Figure 6 displays the diagram for the *Y*-axis nonlinear friction. The related system parameters are shown as follows: R_m=16 Ω, L_m=0.027 H, K_F=86 N/A, K_B=116.6 N/A, M_1=1.205 kg, M_2=1.2 kg, M_3=4.006 kg, C_1=110 N·s/m, C_2=110 N·s/m,, K_1=2.6×10^7 N/m, K_{eq}=1.2×10^5 N/m, F_c=11 N, F_{st}=9 N, v_s=0.004 m/s, and μ=120 N·s/m.

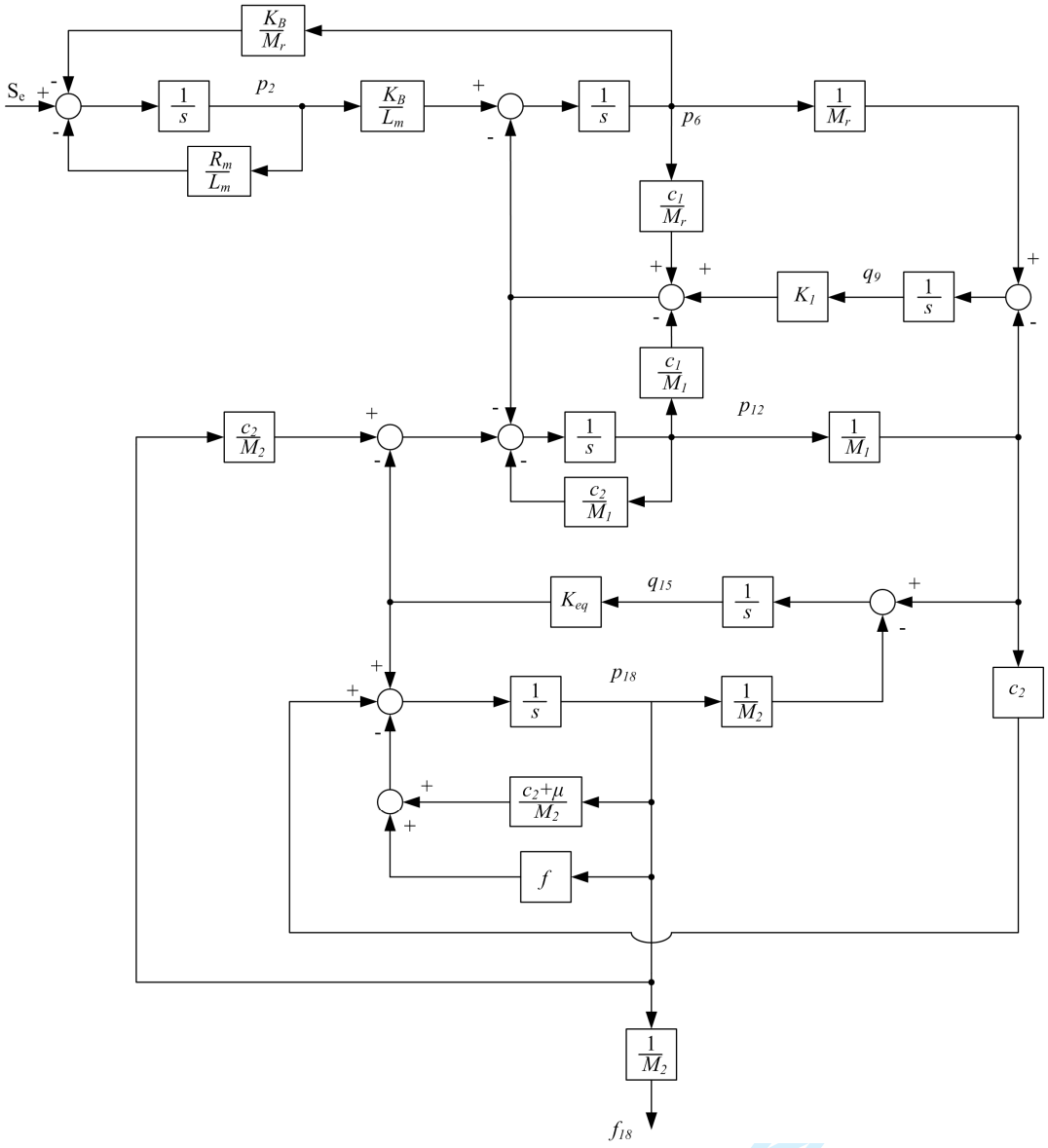

Fig.5 The global system control diagram for *Y*-axis servomechanism.

3 Controller design

A model-based control methodology is presented to control the *XY* stage. In order to reduce the deviations of displacement, velocity and acceleration in terms of force compensation, the controller is realized through transforming the forces applied to the VCM coil and tables to the control voltage signals. The cascaded control structure including three closed-loops is adopted. For *X*-axis servomechanism, the PWM servo

driver is used, and its transfer function is given as follow

$$G_{PWM}(s) = K_s / (T_s s + 1) \qquad (20)$$

where K_s is the gain of the PWM driver, T_s is time constant, and s is differential operator.

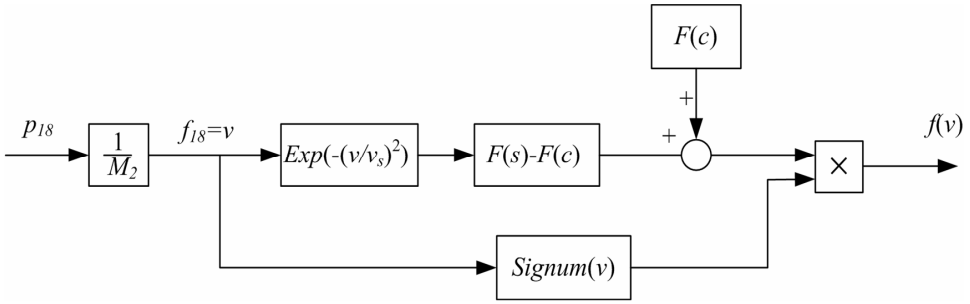

Fig.6 The control diagram for *Y*-axis nonlinear friction.

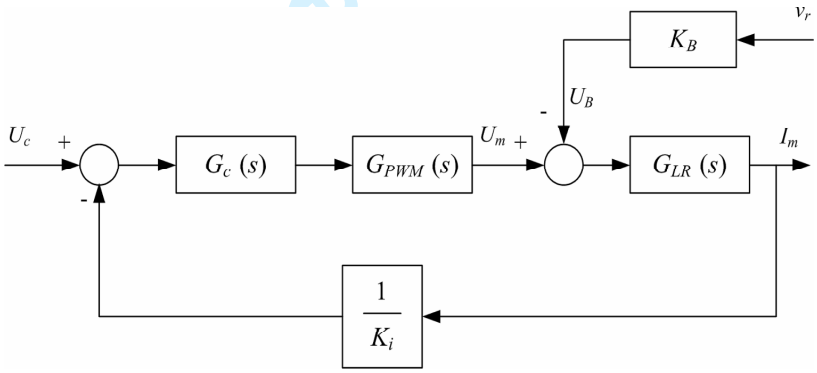

Fig.7 The current loop control diagram of the controller.

The control voltage is transformed to the current of the VCM through current loop, and its control diagram is shown in Fig.7, where U_c is the input control voltage, $G_c(s)$ is the transfer function of current loop PID controller, $1/K_i$ is the current conversion factor, U_m is the operating voltage of VCM coil, U_B is the back electromotive force of the VCM coil, $G_{LR}(s)$ is the equivalent transfer function of the VCM, and I_m is the current of VCM coil.

The inertia force and friction are compensated in the current loop, and the control

diagram is displayed in Fig.8, where a_r is the acceleration of VCM coil, $G_a(s)$ and $G_f(s)$ are the transfer functions of the inertia force and friction compensators, $G_a(s)=K_a$, $G_f(s)=K_F$, K_a and K_f are constants, U_a and U_f are the control voltages of the inertia force and friction compensators, respectively. Thus the following equations can be obtained.

$$U_a = a_r \cdot G_a(s) = a_r \cdot K_a = (K_a \cdot F_{i1}) / M_r \qquad (21)$$

$$U_f = signum(v_r) \cdot G_f(s) = signum(v_r) \cdot K_F \qquad (22)$$

$$U_m = I_m / K_i = F_m / (K_i \cdot K_f) \qquad (23)$$

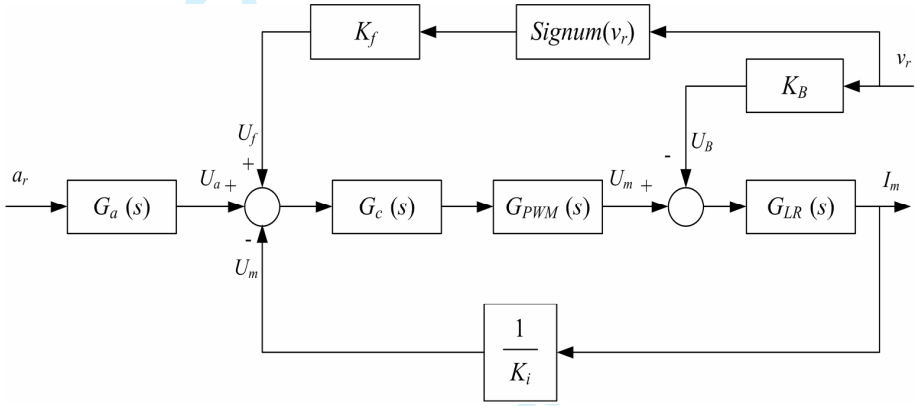

Fig.8 The control diagram for inertia force and friction compensations.

The equivalent X-axis damping force can be compensated in the velocity closed-loop, and the control diagram for the X-axis damping force compensation is shown in Fig.9, where v_2 is the velocity feedback, K_{v0} is the velocity feedback coefficient, K_{v1} is the velocity gain of VCM coil, $G_v(s)$ is the transfer function of damping force compensator and $G_v(s)=K_v$, K_v is a constant. The damping force compensation is realized through transforming the damping force to the voltage as the input of the current closed-loop, and it can be calculated as

$$U_v = G_v(s) \cdot (K_{v1} v_r - K_{v0} v_2) \qquad (24)$$

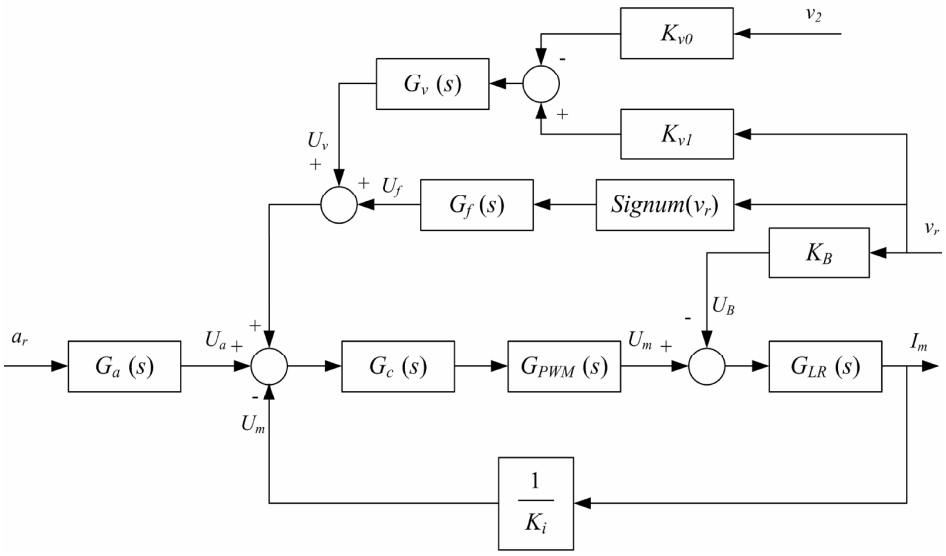

Fig.9 The control diagram for the *X*-axis damping force compensation

When $K_{v0}=K_{v1}$, Eq.(24) yields

$$U_v = K_v K_{v0}(v_r - v_2) = K_v K_{v0} F_d / C_1 \quad (25)$$

where F_d is the damping force.

The equivalent *X*-axis spring force is compensated in the position closed-loop, and the control diagram for the *X*-axis spring force compensation is shown in Fig.10, where x_1 and x_2 are the displacements of *X*-axis VCM coil and table, respectively, $G_p(s)$ is the transfer function of spring force compensator and $G_p(s)=K_p$, K_p is a constant. The control voltage for the spring force compensation can be expressed as

$$U_p = G_p(s)\cdot(x_r - x_2) = (K_p \cdot F_s)/K_1 \quad (26)$$

where F_s is the equivalent spring force.

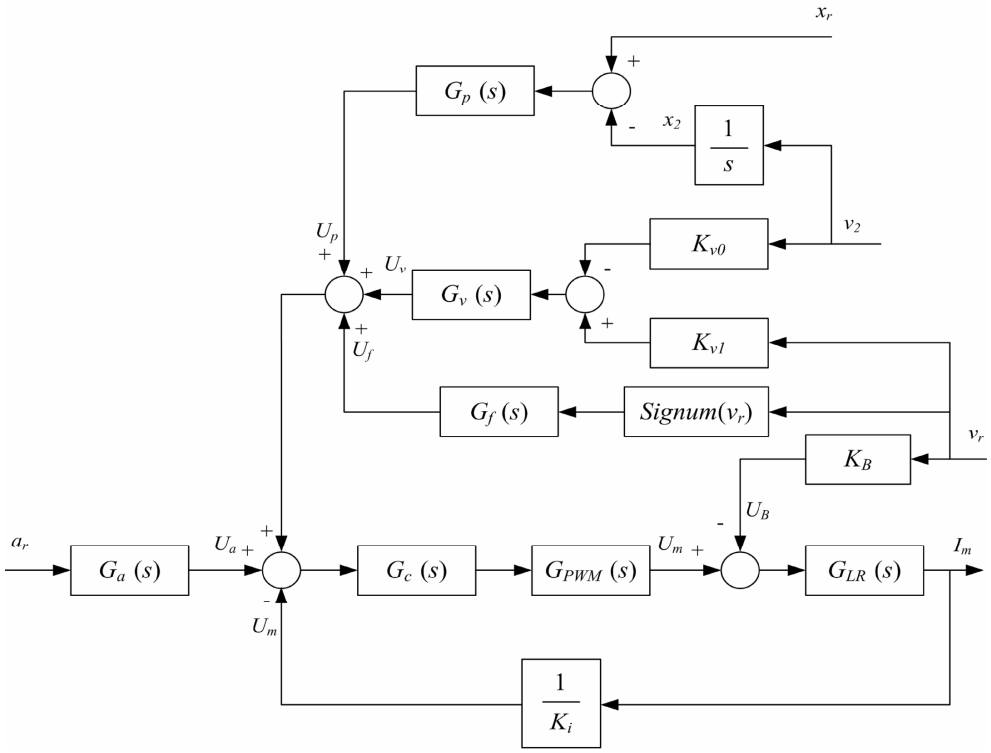

Fig.10 The control diagram for the *X*-axis damping force compensation

Taking the motion parameters of *X*-axis VCM coil as the reference commands, the control diagram for *X*-axis force compensation is obtained, and it is depicted in Fig.11. The integral of displacement following error is used to eliminate the position steady error. The response stiffness of the servomechanism is determined by the performance of the spring force compensator. The damping characteristics of the servomechanism are determined by the performance of the damping force compensator, and the displacement following error related to the speed can be eliminated, meanwhile the overshot is reduced by increasing the gain of the compensator. The displacement following error related to the acceleration can be eliminated by the inertia force compensator, and the frictional effect can be reduced by the friction compensator.

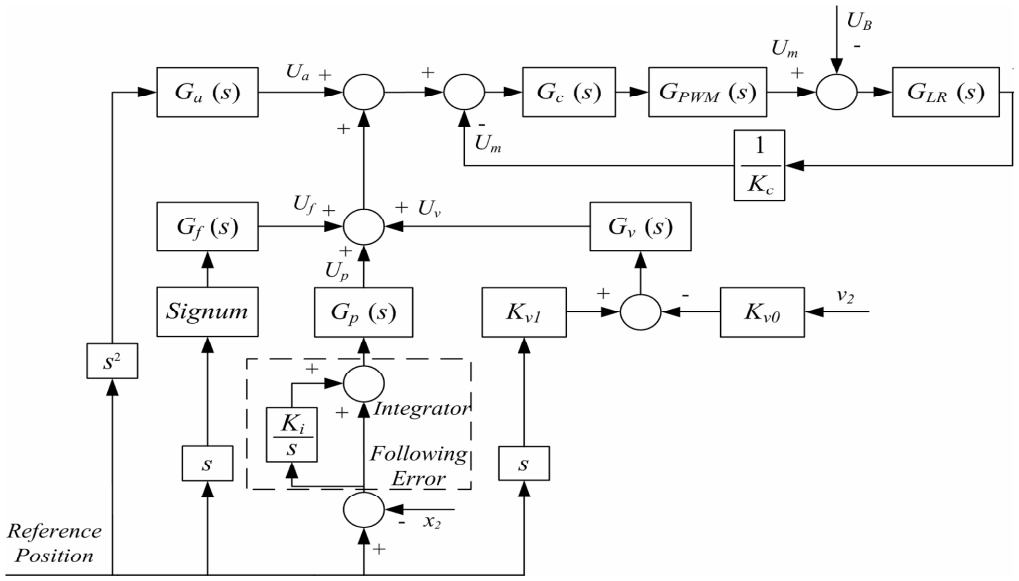

Fig.11 The control diagram for *X*-axis force compensation

The main parameters of the controller are determined by

$$K_a = M_r /(K_i \cdot K_f) \qquad (27)$$

$$K_F = F_c /(K_i \cdot K_f) \qquad (28)$$

$$K_v \cdot K_{v0} = C_1 /(K_i \cdot K_f) \qquad (29)$$

$$K_p = K_1 /(K_i \cdot K_f) \qquad (30)$$

The *Y*-axis controller design process is similar to the *X*-axis. According to the bond graph of *Y*-axis servomechanism, the following equation can be obtained.

$$F_L = F_{i1y} + F_{dy} + F_{sy} + F_{F1y} \qquad (31)$$

Thus

$$F_L = M_r a_r + C_2 (v_r - v_2) + K_{eq}(y_1 - y_2) + \mu v_r \qquad (32)$$

Based on the principle of force compensator, the following equations can be got.

$$U_a = a_r \cdot G_a(s) = a_r \cdot K_a \qquad (33)$$

$$U_f = signum(v_r) \cdot G_f(s) = signum(v_r) \cdot K_F \qquad (34)$$

$$U_v = G_v(s) \cdot (K_{v1} v_r - K_{v0} v_2) \qquad (35)$$

$$U_p = G_p(s)\cdot(y_r - y_2) = K_p\cdot(y_r - y_2) \qquad (36)$$

The main parameters of *Y*-axis controller can be calculated by equations (27)-(30).

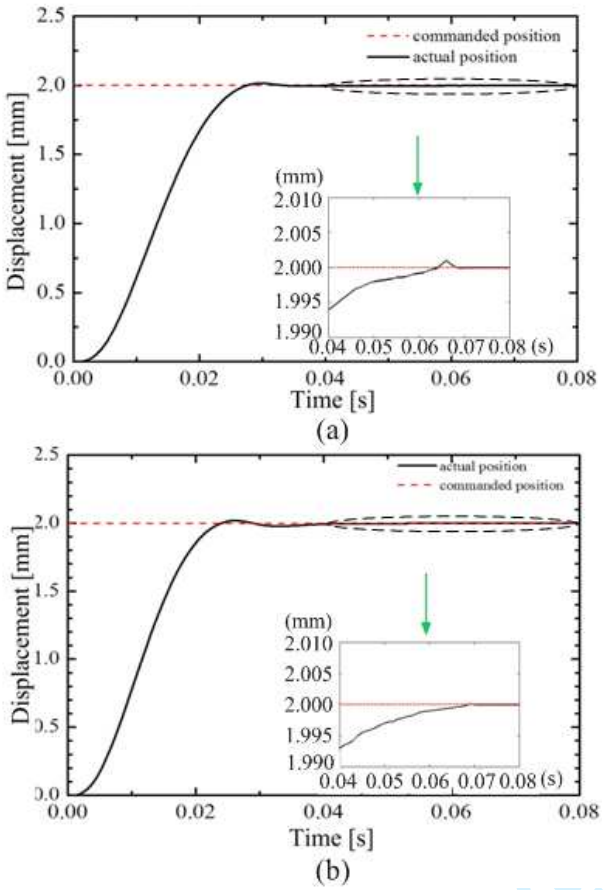

Fig.12 Simulation results for the motion of the *XY* stage: (a) for *X*-axis, and (b) for *Y*-axis.

Simulations are carried out using MATLAB/SIMULINK software to investigate the performance of the controllers. **For *X*-axis controller, K_a=0.5, K_F=5, K_v=2 and K_p=21, and for *Y*-axis controller, K_a=0.6, K_F=9, K_v=3 and K_p=15.** The reference displacement is defined as 2 mm. and the simulation results of step responses are shown in Fig.12. It can be seen that the *X*-axis settling time of the motion is 63 ms, the overshoot is 1.1%, and the steady-state error of

displacement is ±1.5 μm. The *Y*-axis settling time of the motion is 65 ms, the overshoot is 0.5%, and the steady-state error of displacement is ±1.5 μm.

4 Experiments

Experiments are carried out to examine the performance of the *XY* stage, and the experimental setup is shown in Fig.13. SMAC LAL300 VCMs are adopted as the drivers of the *XY* stage. The RENISHAW RGH22 linear grating encoders are used as the feedback sensors for *X*- and *Y*-axes tables. The implementation of the controller is realized through Turbo PMAC2 PCI motion control card. A RENISHAW EC10/ML10 laser interferometer is utilized to investigate the characteristics of the stage. To reduce the influences caused by the vibration and noise from the ground surface, the system is placed on a Newport RS-4000 vibration isolating table with air bearings.

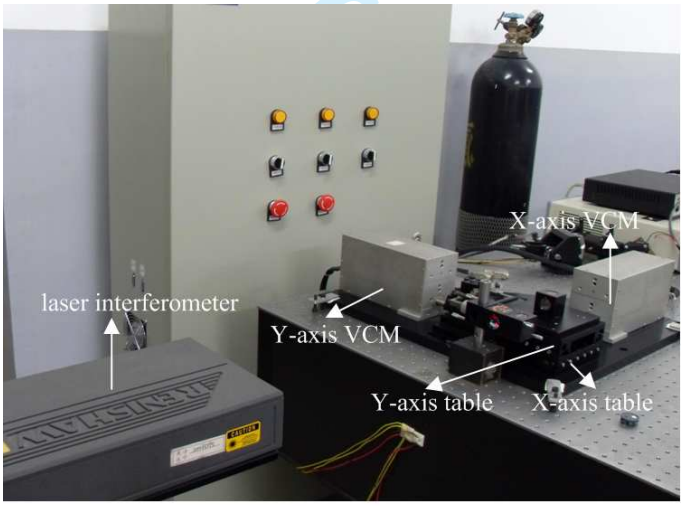

Fig.13 The experimental setup.

Fig.14 provides the step responses of *X*-axis and *Y*-axis tables. **Based on the simulation parameter values of the controller, the actual parameter tuning are carried out. There are only four parameters to be tuned, and the control algorithm is simple, thus reducing the calculation cost. Finally the parameter values are**

determined. For *X*-axis controller, K_a=0.6, K_F=7, K_v=5 and K_p=16, and for *Y*-axis controller, K_a=0.8, K_F=8, K_v=5 and K_p=12. The ± 1.5 μm band at the desired level is used as the acceptable range of variation from the desired response, and thus the *X*-axis table settling time is found to be 64 ms, the overshoot is 0.7%. *Y*-axis table settling time is 62 ms, and the overshoot is 0.8%.

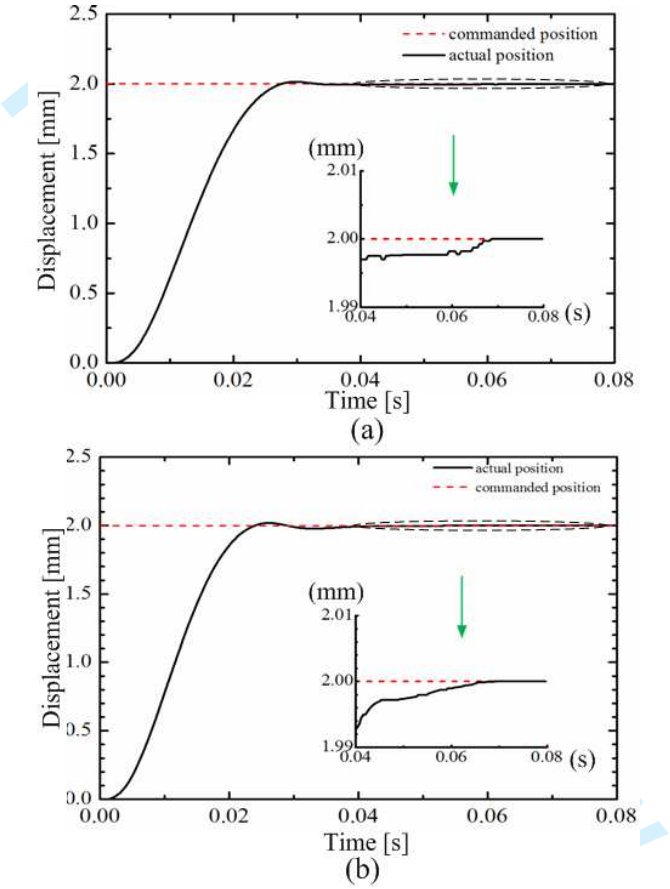

Fig.14 The step responses of the *XY* stage: (a) for *X*-axis, and (b) for *Y*-axis.

The parabola velocity response curves are shown in Fig.15. It can be concluded that the actual position curves can match well with the command positions. The *X*-axis dynamic position tracking errors are within ± 2.5 μm and the *Y*-axis dynamic position tracking errors are within ± 4 μm. The simulation results are in a good agreement with the experimental results, which proves the correctness of the theoretical model.

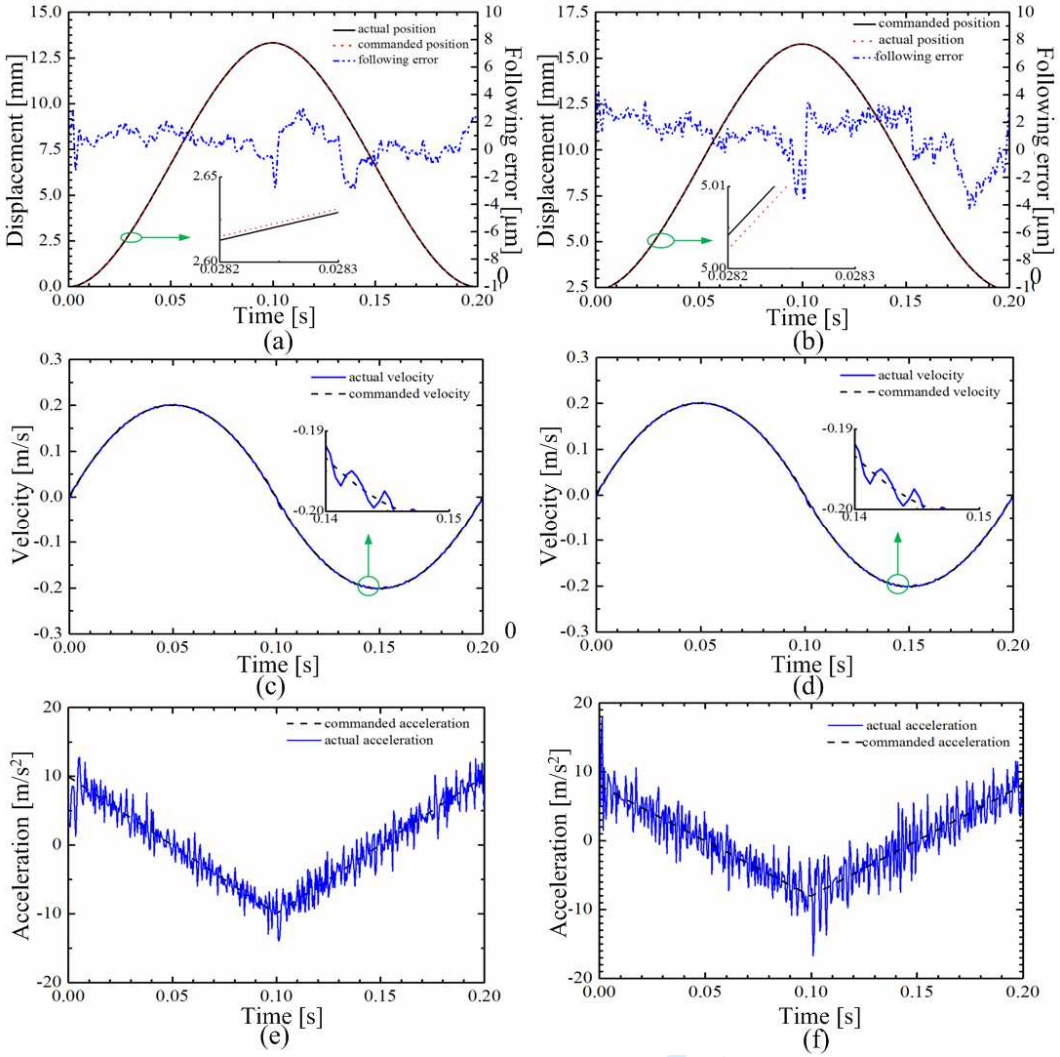

Fig.15 The parabola velocity response curves: (a) *X*-axis displacement, (b) *Y*-axis displacement, (c) *X*-axis velocity, (d) *Y*-axis velocity, (e) *X*-axis acceleration, and (f) *Y*-axis acceleration.

For the positioning accuracy and repeated positioning accuracy, the ISO standard for the *XY* stage of machine tools is adopted, and it is measured using the RENISHAW laser interferometer, and then the data is processed using RENISHAW software. Motion range of 12 mm is divided into six segments by seven points. When the table moves with the step size of 2 mm, laser interferometer measures the displacement errors of the seven points, and five motion cycles are operated, and

thus ten displacement errors are recorded in all at every point. Thus, the positioning accuracy and repeatability of the *X*-axis and *Y*-axis can be obtained using the recorded data. The recorded data are plotted in Fig.16. Forward stroke displacement error curve is expressed by continuous line, and backward stroke displacement error curve is described by dashed line. The results indicate that *X*-axis positioning accuracy is 1.75 μm, and the repeatability is 0.9 μm. *Y*-axis positioning accuracy and repeatability are 1.5 μm and 0.8 μm, respectively.

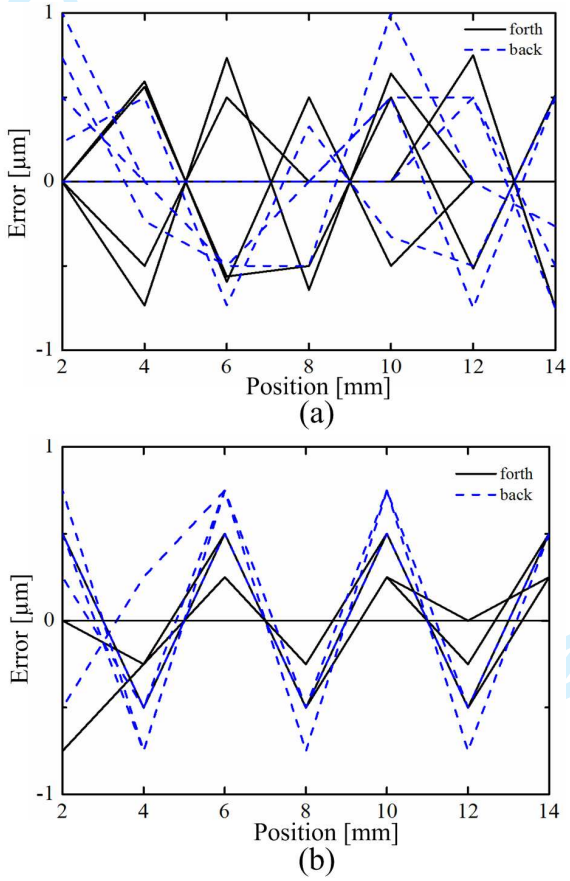

Fig.16 The positioning accuracy and repeatability: (a) for *X*-axis; and (b) for *Y*-axis.

The *X*- and *Y*-axes positioning accuracy has been simultaneously measured across the entire workspace. The results show that *X*-axis positioning accuracy is 1.85 μm, and the repeatability is 0.95 μm. *Y*-axis positioning accuracy and

repeatability are 1.75 μm and 0.9 μm, respectively.

The main performance indexes of the *XY* stage are tested and summarized in Table 1.

Table 1 The main performance indexes of the XY stage

	Repeating positioning accuracy (μm)	Maximum speed (m/s)	Resolution (μm)	Motion stroke (mm)
X-axis	0.95	0.45	0.5	50
Y-axis	0.9	0.62	0.5	50

2-DOF trajectory tracking experiments have also been performed to investigate the tracking performance of the *XY* stage, and **the dynamic tracking errors of all the points is used to describe the trajectory tracking performance of the *XY* stage.** Figure 17 plots the tracking results of the linear trajectory with an obliquity of 45°. From Fig.17, it is seen that the actual trajectory almost coincides with the desired trajectory, and there is a little delay of *Y*-axis motion compared with *X*-axis motion in the positive motion, while in the negative motion, there is a little delay of *X*-axis motion compared with *Y*-axis motion.

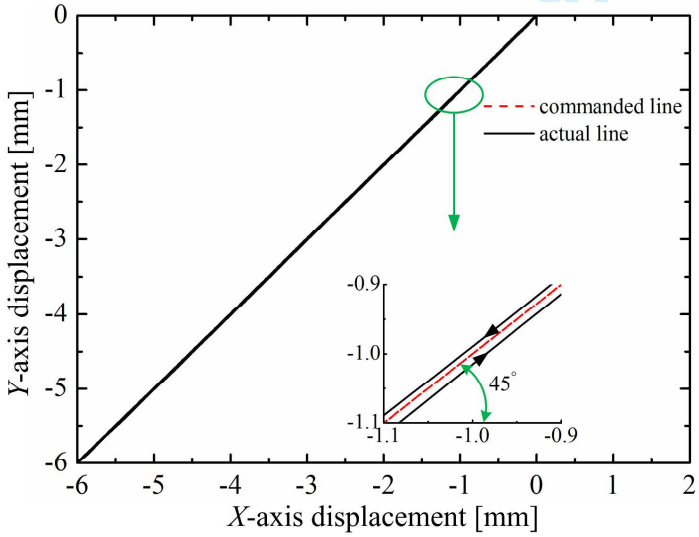

Fig.17 The tracking results of the linear trajectory.

Planar circular trajectories are also chosen as the desired trajectories, and the displacements of the stage with different displacement commands are plotted in Fig.18, where the diameters of the two command circles are 16 mm and 4 mm, respectively. It is known from Fig.18 that the actual trajectories can track the desired circular trajectories well, and the result shows that the *X*-axis dynamic position tracking errors are within ± 2.5μm and the *Y*-axis dynamic position tracking errors are within ± 3.0 μm.

The capability of tracking more complex trajectory is further examined, and the following smooth trajectory is chosen as the reference trajectory.

$$\begin{aligned} x_r &= 4\sin(\pi t - 0.5\pi) + 2\sin(8\pi t - 0.5\pi) \\ y_r &= 4\sin(\pi t) + 2\sin(8\pi t) \end{aligned} \qquad (37)$$

where x_r, y_r are the *X*- and *Y*- axes command displacements, respectively, and t is time.

The trajectory tracking result is displayed in Fig.19, which shows that the stage can track the smooth trajectory well. During the motion process, the *X*-axis dynamic position tracking errors are within ± 2.5μm and the *Y*-axis dynamic position tracking errors are within ± 3.5 μm.

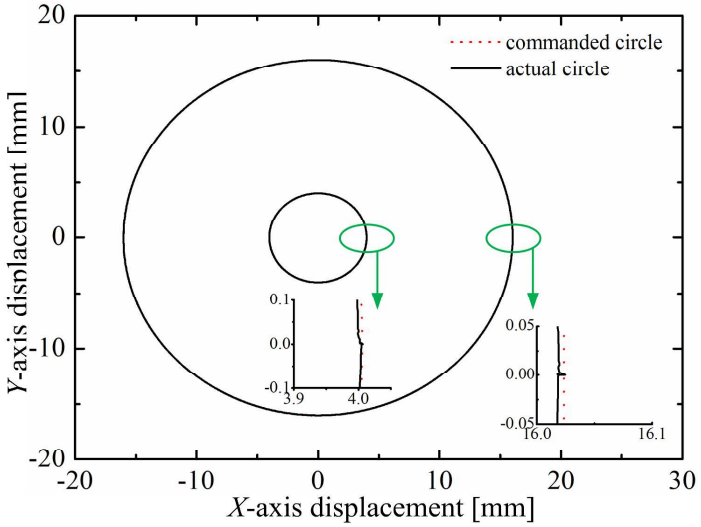

Fig.18 The tracking results of different reference circular trajectory.

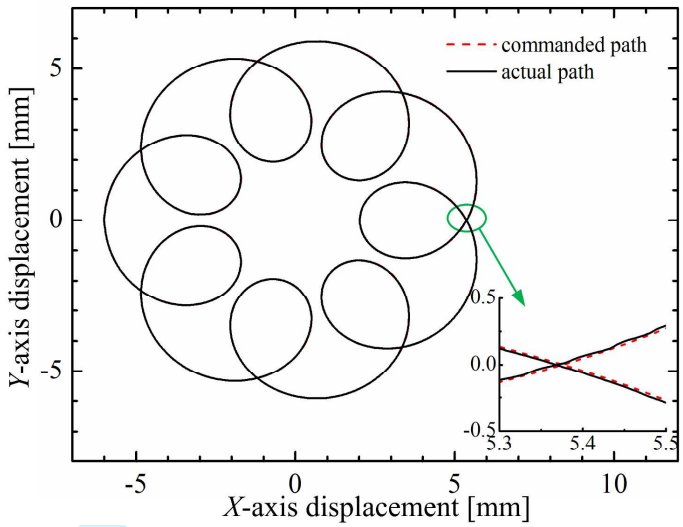

Fig.19 The trajectory tracking of the smooth trajectory.

5 Conclusions

To improve the quality and efficiency of semiconductor packaging, the dynamic modeling, controller design and experimental tests of a LVCM direct-drive *XY* positioning stage are carried out in this paper. Based on the characteristics of the servomechanisms of the *XY* stage, the bond graphs of the stage are established, and the state space equations are obtained. The controller based on force compensations is proposed to control the *XY* stage, and it is realized through transforming the forces that applied to the VCM coil and tables to the control voltage signals. The performance of the *XY* stage are evaluated by experimental tests. The results show that when the reference displacements are defined as 2 mm, the settling time of the *X*-axis movement is 64 ms, and the overshoot is 0.7%. *Y*-axis settling time is 62 ms, and the overshoot is 0.8%. *X*-axis positioning accuracy is 1.85 μm, and the repeatability is 0.95 μm. *Y*-axis positioning accuracy and repeatability are 1.75 μm and 0.9 μm, respectively. The linear, circular and complex curve trajectory experimental results indicate the trajectory

tracking performance of the *XY* stage are very well.

Acknowledgements

The supports of this work by the National Natural Science Foundation of China (Grant no. 51205279 and 51175372), and the Science & Technology Commission of Tianjin Municipality (Grant no. 13JCQNJC04100), the Tianjin University for Peiyang Elite Scholar (Grant no. 60301014) and CSC Scholarship are gratefully acknowledged.

References

1 Adamy J, Flemming A (2004) Soft variable-structure controls: A survey. Automatica 40:1821-1844

2 Aized T, Shirinzadeh B (2011) Robotic fiber placement process analysis and optimization using response surface method. Int J Adv Manuf Technol 55:393-404

3 Ang K H, Chong G, Li Y (2005) PID control system analysis, design, and technology. IEEE Trans Control Syst Technol 13:559-576

4 Cai T, Zhang M, Zhu Y, Hu C (2011) Dynamic modeling and analysis of a 3-DOF ultra-precision positioning stage with air bearing. Procedia Eng 16:264-270

5 Dejima S, Gao W, Katakura K, Kiyono S, Tomita Y (2005) Dynamic modeling, controller design and experimental validation of a planar motion stage for precision positioning. Precis Eng 29:263-271

6 Fatikow S, Eichhorn V, Stolle, C, Sievers T, Jahnisch M (2008). Development and control of a versatile nanohandling robot cell. Mechatronics. 18(7):370-80.

7 Ferreira P M, Qing Y, Dong J (2007) Design, analysis, fabrication and testing of a parallel-kinematic micropositioning *XY* stage. Int J Mach Tools Manuf 47:946-961

8 Fung R-F; Hsu Y-L, Huang M-S (2009) System identification of a dual-stage XY precision positioning table. Precis Eng 33:71-80

9 Hace A, Jezernik K, Curk B, Terbuc M (1998) Robust motion control of *XY* table for laser cutting machine. Proceedings of the 1998 24th Annual Conference of the IEEE Industrial Electronics Society, Aachen, Germany, pp 1097-1102

10 Hwang J, Park C-H, Kim S-W (2010) Estimation method for errors of an aerostatic planar *XY* stage based on measured profiles errors. Int J Adv Manuf Technol 46:877-883

11 Khan M U, Bencheikh N, Prelle C, Lamarque F, Beutel T, Buttgenbach S (2012) A long stroke electromagnetic *XY* positioning stage for micro applications. IEEE ASME Trans Mechatron, 17(5): 866-875

12 Li YM, Xu Q S (2011). A novel piezoactuated *XY* stage with parallel, decoupled, and stacked flexure structure for micro-/nanopositioning. IEEE Trans Ind Electron. 58:3601-3615

13 Li Y M, Xu Q S (2012) Design and robust repetitive control of a new parallel-kinematic *XY* piezostage for micro/nanomanipulation. IEEE/ASME Trans Mechatronics, 17(6): 1120-1131

14 Liang Q, Zhang D, Song Q, Ge Y (2010) Design of a compliant *XY* stage with embedded force sensor for micro-scale positioning. Proceedings of 2010 IEEE International Conference on Information and Automation, Harbin, China, pp 1494-1499

15 Liaw HC, Shirinzadeh B, Smith J (2008). A Robust motion tracking control of piezo-driven flexure-based four-bar mechanism for micro/nano manipulation. Mechatronics. 18(2):111-20.

16 Liu Z Z, Luo F L, Rahman M A (2005) Robust and precision motion control system of linear-motor direct drive for high-speed X-Y table positioning mechanism. IEEE Trans Ind Electron 52:1357-1363

17 Liu Z Z, Luo F L, Rashid M H (2003) QFT-based robust and precision motion control system for a high speed direct-drive *XY* table positioning mechanism. Proceedings of the IEEE Industry Applications Conference, UT, USA, pp 293–300

18 Mou S-C, Sung C-H (2012) Fuzzy positioning control of the novel single-axis piezoelectric actuated stage. Proceedings of 2012 International Symposium on Computer, Consumer and Control, Taichung, Taiwan, pp 771-776

19 Sanchez-Salmeron A J, Ricolfe-Viala C (2012) A flexible packaging station for micro-bulk-forming applications based on a standard carrier. Int J Adv Manuf Technol 61:529-536

20 Sun L, Li T, Liu Y (2011) Modeling and analysis of a high acceleration and precision linear motor direct drive motion stage with bond graph approach. Robot 33:467-474

21 Teo C S, Tan K K, Lim S Y, Huang S, Tay E B (2007) Dynamic modeling and adaptive control of a H-type gantry stage. Mechatronics 17:361-367

22 Tian Y, Shirinzadeh B, Zhang D (2009) A flexure-based mechanism and control methodology for ultra-precision turning operation. Precis Eng 33:160-166

23 Tomizuka M (1987) Zero phase error tracking algorithm for digital control. J Dyn Syst Meas Control Trans ASME 190:65-68

24 Wang F, Li J, Liu S, Zhao X, Zhang D, Tian Y (2014) An improved adaptive genetic algorithm for image segmentation and vision alignment used in microelectronic bonding, IEEE/ASME Transactions on Mechatronics. 19(3): 916-923

25 Wang F, Zhao X, Zhang D, Ma Z, Jing X (2011) Robust and precision motion control for a directly driven XY table, Proceedings of IMechE, Part C, Journal of Mechanical Engineering Science. 225(5): 1107-1120

26 Wang F, Zhao X, Zhang D, Wu Y (2009) Development of novel ultrasonic transducers for microelectronics packaging, Journal of Materials Processing Technology. 209(3): 1291-1301

27 Wang W, Shin D, Han C, Choi H (2009) Modeling and simulation for dual stage system using bond graph theory. Proceedings of International Symposium on Optomechatronic Technologies, Istanbul, Turkey, pp 197-202

28 Wang Y, Xiong Z H, Ding H (2006) Robust controller based on friction compensation and disturbance observer for a motion platform driven by a linear motor. Proc IMechE Part I: J Syst Control Eng 220:33-39

29 Wu Y T, Ding H (2007) Reference adjustment for a high-acceleration and high-precision platform via A-type of iterative learning control. Proc IMechE Part I: J Syst Control Eng, 221:781-789

30 Xu L, Yao B (2000) Coordinated adaptive robust contour tracking of linear-motor-driven tables in task space. Proceedings of the IEEE Conference on Decision and Control, Sydney, Australia, pp. 2430-2435

31 Xu Q S, Li Y M (2009) Radial basis function neural network control of an *XY* micropositioning stage without exact dynamic model. Proceedings of 2009 IEEE/ASME International Conference on Advanced Intelligent Mechatronics, Singapore, pp. 498-503

32 Zhang H, Wang F, Zhao X, Zhang D, Tian Y (2013) Electrical matching of a piezoelectric ultrasonic transducer for microelectronic bonding, Sensors and Actuators A: Physical. 199(1): 241-249

33 Zhao Y, Yang K, Zhu Y, Pan S (2010) Modeling and analyzing of an H-drive precision *XY* stage. Proceedings of 2010 International Conference on Mechanic Automation and Control Engineering, Wuhan, China, pp 6311-6314

APPENDIX

Notation

a_r acceleration of VCM coil

$\boldsymbol{C}$ capacitor element

C_1 damping between coil and the guiding fin

C_2 equivalent damping between the Y-axis guiding fin and table

e effort

f flow

F force generated by the VCM

F_c coulomb friction

F_d damping force

F_{dy} Y-axis damping force

F_{F1} friction of the X-axis coil

F_{F1y} friction of the Y-axis coil

F_{F2} friction of the X-axis table

F_{F2y} friction of the Y-axis table

F_{i1} inertia force of the X-axis coil

F_{i1y} inertia force of the Y-axis coil

F_{i2} inertia force of the X-axis table

F_{i2y} inertia force of the Y-axis table

F_L output force of the coil

F_s equivalent spring force

F_{st} static friction

F_{sy} Y-axis equivalent spring force

$G_a(s)$ transfer function of the inertia force

$G_c(s)$ transfer function of current loop PID controller,

$G_f(s)$ transfer function of friction compensator

$G_v(s)$ transfer function of damping force compensator

$G_p(s)$ transfer function of spring force compensator

$G_{LR}(s)$ equivalent transfer function of the VCM

i current intensity through the coil

I_m current of VCM coil

K	stiffness of the preload spring
K_1	connecting stiffness between coil and the guiding fin
K_c	contact stiffness between the bearing and the lapping plate
$1/K_i$	current conversion factor
K_s	gain of the PWM driver
K_t	stiffness of the flexure hinge
K_{v0}	velocity feedback coefficient
K_{v1}	velocity gain of VCM coil
K_B	coefficient of inducted electromotive force
K_F	force coefficient.
L_m	inductance of the VCM coil
M_1	equivalent mass of the *Y*-axis guiding fin
M_2	equivalent mass of the *Y*-axis table
M_3	mass of the *X*-axis table
M_r	mass of the coil
$p(t)$)	time integral of effort
$q(t)$	time integral of flow
$\boldsymbol{R}$	resistor elements
R_m	resistance of the VCM coil
s	differential operator
$\boldsymbol{S}_e$	effort source
T_s	time constant
$\boldsymbol{u}_x$	input variable
U	voltage applied to the VCM
U_a	control voltage of the inertia force
U_c	input control voltage
U_f	control voltage of friction compensator
U_B	back electromotive force of the VCM coil
U_m	operating voltage of VCM coil
v	motion velocity of the VCM coil
v_2	velocity feedback
v_f	velocity
v_s	Stribeck velocity
x	displacement of *X*-axis table